FULL RESEARCH ARTICLE

Sintering behaviour of 3D-printed 18K 5N gold alloy by binder jetting: a preliminary study

Marco Mariani[1] · Tiziana Vario[1] · Karim Salaheldin[1] · Massimiliano Annoni[1] · Nora Lecis[1]

Abstract

Binder jetting is a versatile additive manufacturing technique suitable to produce alloys that are difficult to obtain by powder bed fusion techniques, such as precious metals, due to their high reflectivity and thermal conductivity. In this study, a 18K 5N gold alloy powder was employed in the printing process. Different heat treatments and densification processes were employed to achieve final-stage sintering and remove residual porosity, whilst controlling the evolution of copper oxides by reduction with hydrogen and graphite. Powder, green and sintered samples were characterised at the microstructural level by X-ray diffraction, microscopy and energy dispersive X-ray spectroscopy to assess phase transitions and secondary-phase formation. Oxide-free components with a final relative density above 90% were achieved by densification at 830 °C combined with carbon- and CO-induced reduction of tenorite and cuprite. The optimal manufacturing route was chosen to produce a bezel, as a case study for the adoption of this technique in the jewellery industry.

Keywords Binder jetting · Gold alloy · Additive manufacturing · Sintering · Copper oxides · Reduction

1 Introduction

Precious metals, as gold, silver and platinum, are interesting materials for the application of additive manufacturing (AM) techniques because they are correlated to the production of customised high-added value products, typical of industrial sectors as jewellery and dentistry [1, 2]. In both cases, unique designs and solutions are highly regarded given the importance of aesthetic in the first case [3] and tailored configurations in the second [4, 5].

In the metal AM scenario, the most developed processes are powder bed fusion (PBF) and direct energy deposition (DED) with a laser source. Such techniques are suitable for most metals; however, the high reflectivity and thermal conductivity of some materials (e.g. gold, silver, copper…) place a series of challenges to the achievement of dense and precise components since melting pools are reduced in size and unstable. In addition, all the usual disadvantages of direct AM processes must be accounted for: strong microstructural anisotropy [6], low control on phase

transformations [7], building up of residual stresses, presence of residual porosity [5, 8, 9], need for support structures and others. In the past decade, several efforts explored the possibility of producing components from L-PBF, but limited advancements were obtained.

In the last years, AM of metals has seen the rise of indirect techniques based on a shaping phase followed by a sintering process to achieve densification as in the case of binder jetting (BJT) and material extrusion. In particular, BJT features an almost unlimited freedom of design and employs feedstocks that can be produced rapidly with a multitude of processes (for example gas or ultrasonic atomisation); thus, it could be easily applied to the aforementioned industrial necessities.

Given the absence of scientific publications on precious metals by BJT, the work is aimed at investigating all the steps of production of 18 karats gold alloy with a focus on phase transformations and redox reactions undergoing the different treatments involved in the process.

✉ Marco Mariani
  marco.mariani@polimi.it

1 Department of Mechanical Engineering, Politecnico di Milano, via La Masa 1, 20156 Milan, Italy

2 Materials and methods

2.1 Printing parameters and sintering procedures

The feedstock material was a spherical 18K 5N gold alloy powder (Fig. 1) provided by Legor (IT) with a $D_{50} = 10.8$ µm (sieved at 25 µm) and a Carr index of 8.11. The liquid binder of choice was the AquaFuse® from ExOne (US), which is an aqueous-based solution containing the monomers for polyethylene glycol (PEG) formation.

The studied specimens were printed with an Innovent + machine from ExOne (US). The printing parameters were optimised to allow the deposition of a sufficient amount of material to generate a compact powder bed and they are listed in Table 1. The curing phase was performed at 180 °C for 6 h to achieve the crosslinking of the polymeric phase in the deposited liquid binder, thus allowing

the extraction of the green bodies from the excess powder by manual brushing.

The sintering behaviour was initially studied by dilatometry performed in a LINSEIS DIL L75 PT dilatometer. Both green (cured) and brown (debinded) samples were analysed in inert atmosphere (Ar) following the thermal treatments described in Table 2.

Then, debinding and sintering were performed in a single cycle in a dedicated furnace. Debinding was achieved by adding an initial step of 3 h at 450 °C, to complete the burn-out of the organic phase, whilst sintering was attempted at different temperatures and atmospheres, as listed in Table 2, to verify which conditions were beneficial to densification and geometrical accuracy. "RX" (X = dwelling temperature) is used for referring to the samples treated in a reducing atmosphere. "IX" refers to the treatments performed with inert atmosphere (Ar) in a graphite crucible to promote carbon monoxide/dioxide formation.

Fig. 1 SEM image (left) and cumulative distribution (right) of the gas atomised powder from a 18K 5N gold alloy
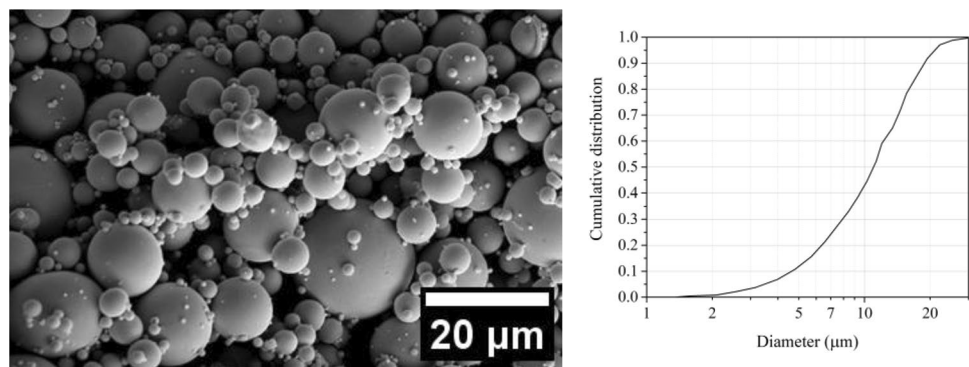
Table 1 Printing parameters employed to produce the specimens

Binder set time (s)	Drying time (s)	Bed temperature (°C)	Roller speed (rpm)	Recoat speed (mm s^{-1})	Layer thickness (µm)	Binder saturation (%)
5.0	15.0	50.0	600	3.0	50	80

Table 2 Debinding and sintering conditions applied during dilatometric analysis, respectively, on cured (green) and debinded (brown) samples, and thermal treatments performed to achieve densification (RX, IX)

Sample ID	Heating rate (°C min^{-1})	Debinding temperature (°C)	Debinding time (h)	Sintering temperature (°C)	Sintering time (h)	Atmosphere
Green	3	450	3	700	3	Ar
Brown	–	–	–	700	3	Ar
R800	5	450	3	800	3	5% H$_2$/95% N$_2$
R830	5	450	3	830	3	5% H$_2$/95% N$_2$
I750	5	450	3	750	3	Ar
I800	5	450	3	800	3	Ar
I830	5	450	3	830	3	Ar

2.2 Microstructural and geometrical characterisation

As-received and cured powders were analysed by X-ray diffraction on a 30°–90° range with a step size of 0.02° and a Cu-Kα source through a SmartLab II Rigaku diffractometer. Phase transformations, debinding reactions and sintering mechanisms were evaluated by combining the results from differential scanning calorimetry analysis (DSC) on powder by a Setaram Labsys 1600 and dilatometric measurements on a green sample (diameter = 4 mm) with a LINSEIS DIL L75 PT Vertical VS1600C. In the former case, the thermal cycle was from room temperature to 1150 °C in inert atmosphere (Ar) with a 5 °C min^{-1} heating rate and − 10 °C min^{-1} cooling rate, while in the latter, it went from room temperature to 450 °C and later to 700 °C with 3 h dwelling time at each step and a heating ramp of 5 °C min^{-1}, then cooled at 10 °C min^{-1}, in argon atmosphere.

All sintered components' relative density was estimated by Archimedes density in water, considering a theoretical density of 14.9 g cm^{-3}.

The samples surface was treated by chemical picking with a sulfamic acid solution at 50 °C for 30 min to remove the superficial oxide layer. The specimens were cut along the transversal direction with respect to the layer orientation and mirror polished. The microstructure was analysed by optical microscopy with a Nikon Eclipse L V150NL and by field emission scanning electron microscopy (FE-SEM) with a ZEISS AG-EVO 50 equipped with energy dispersive X-ray spectroscopy (EDX), employed to quantify the content of Au, Cu, Ag and O in the different regions of the components.

As-printed and polished samples' surface roughness was evaluated by Alicona Infinite Focus optical 3D measuring system (polarised light, cutoff wavelength = 250 μm).

3 Results and discussion

3.1 Powder and green samples analysis

The cylindrical samples for dilatometry and the cubic samples featured an average relative density of 58.5 ± 1.5%, which is extremely high for binder jetting typical values when comparable fine powders are employed [10]. This result is likely achieved thanks to the good flowability of the feedstock (Carr Index < 15) and to the layer-by-layer deposition mode that reduces the risk of macropores formation within the powder bed. The second aspect is likely the most beneficial: layerwise deposition and spreading limit the risk of air entrapment within the particles, which, on the contrary, often occurs when handling large amounts of loose fine particles. Such behaviour is also underlined by the low correlation between packing density and rheometric measurements, with both well and bad flowing feedstocks similarly achieving optimal powder bed density (50–60%) as shown in literature [11–15].

Printed samples accuracy was evaluated by geometrical measurements on the cubes, whose theoretical side length is 3 mm. It was observed that along the planar (X and Y axis) and building (Z axis) directions, the offset from the CAD size is different: the dimensions were 3.18 ± 0.03 mm, 3.16 ± 0.03 mm and 3.38 ± 0.17 mm along the X, Y and Z axis, respectively. The vertical direction is that suffering from the largest discrepancy likely due to accumulation of binder at each interlayer region, responsible for the formation of excess porosity [16, 17].

The dilatometric analysis is presented in Fig. 2A. The consistent shrinkage in the 180–200 °C range is the result of binder burnout in the green component as observed in the thermogravimetric analyses performed by Do et al. [18] and Lecis et al. [10], whilst the expansion peak at 385–400 °C in both curves is due to AuCu I (L1$_0$, face-centred tetragonal) to AuCu II (orthorhombic) ordered phases transformation, as expected by DSC measurement (Fig. 2B) and literature [19–21]. At higher temperatures,

Fig. 2 A Dilatometric analysis on green (straight line) and brown (dotted line) samples and **B** DSC analysis on as-received powder
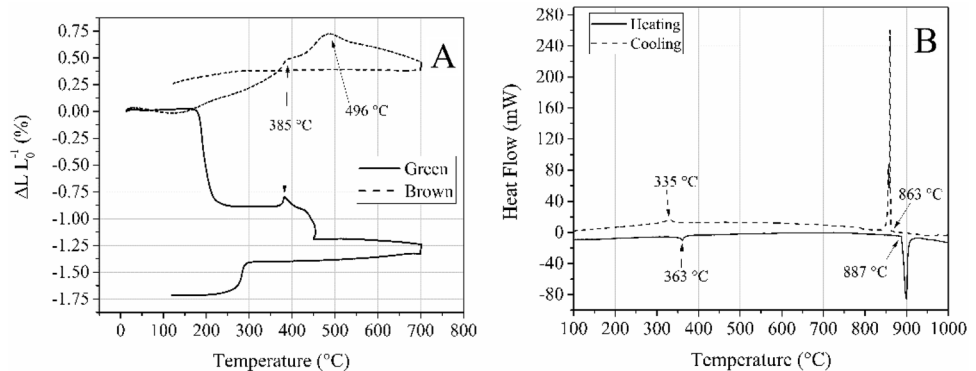
AuCu II transforms into the disordered A1 face-centred cubic phase in correspondence to the Kurnakov point, with gold, silver and copper atoms being progressively solubilised into the solid solution [3, 22]. The volume variation related to the $L1_0$ to A1 transition is confirmed by the lower part of the curve (corresponding to the cooling stage). In this case, the transition onset is below 300 °C likely due to the faster cooling rate which produces a delay amongst the actual beginning of $L1_0$ formation and the detection of the shrinkage. The size reduction during the remaining heating phase of the thermal treatment is moderate and originates from volume diffusion mechanisms initiated at about 500 °C. The analysis on the debinded component underlines that in absence of binder, the part is subject to a relevant increase in size from cumulation of thermal expansion of each particle up to 500 °C. The DSC analysis also sets the onset of liquid-phase formation at about 890 °C, as expected from literature [3, 19].

The phase transformation from $L1_0$ to A1 is confirmed also by XRD analysis on the as-received and cured powders. The as-received powders contain both phases, with residual traces of tenorite (CuO), as can be seen in Fig. 3A [23]. The two phases are likely formed during the atomisation process, whose cooling is fast enough to partially preserve A1, whilst the minimal amount of tenorite is likely the result of oxidation of both phases exposure to air as noted for pure copper by Nyborg and Cao [24], according to the reactions described in Eq. 1 and 2 [20, 25]:

$$L1_0 + \frac{1}{2}O_2 \rightarrow L1_0 + CuO \tag{1}$$

$$A1 + \frac{1}{2}O_2 \rightarrow Au + CuO \tag{2}$$
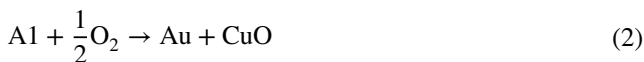
The low-temperature curing process is not responsible for a significant further oxidation of the material, indeed the CuO peaks do not vary significantly; however, the thermal energy provided promotes the minimisation of
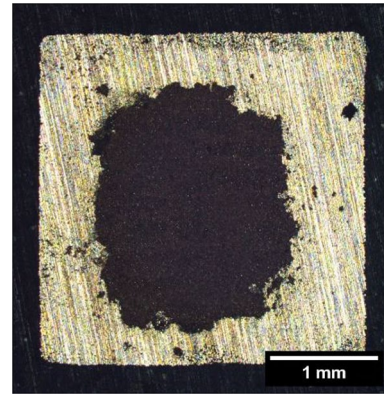
Fig. 4 Optical microscopy of the section of the sintered R830 sample

the residual A1 fraction, thus reducing its characteristic diffraction peaks (46°, 68°, 82°), as shown in Fig. 3B.

3.2 Sintering in reducing atmosphere

Reduction of copper oxides (mainly tenorite, but possibly also traces of cuprite) generated during powder production/handling and curing in air (Eqs. 3 and 4, respectively) is obtained by reaction with hydrogen in reducing atmosphere (Eqs. 5 and 6):

$$Cu + \frac{1}{2}O_2 \rightarrow CuO \tag{3}$$

$$2Cu + \frac{1}{2}O_2 \rightarrow Cu_2O \tag{4}$$

$$CuO + H_2 \rightarrow Cu + H_2O \tag{5}$$

$$Cu_2O + H_2 \rightarrow 2Cu + H_2O \tag{6}$$

However, the densification under hydrogen atmosphere is almost irrelevant both at 800 °C and 830 °C. Indeed, the

Fig. 3 XRD spectra of **A** as-received and **B** cured powders
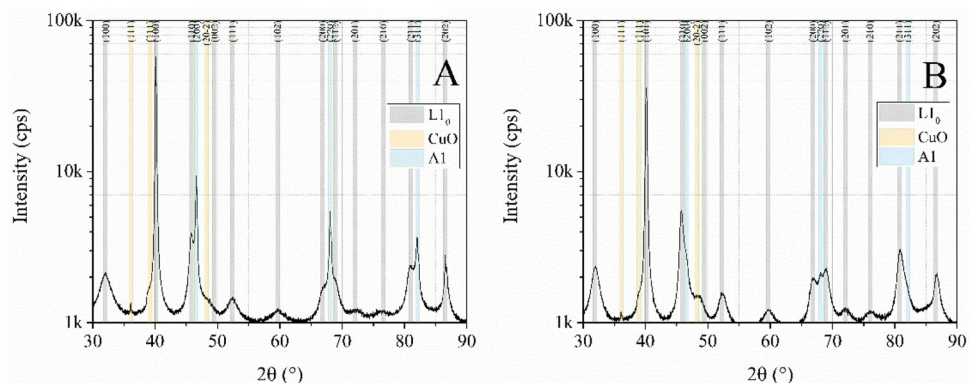
final density is $59.7 \pm 0.8\%$ and $59.6 \pm 0.9\%$ for R800 and R830 samples, respectively. Optical microscopy in Fig. 4 confirms that the sintering cycle induces densification of the outer shell of the printed components; however, shrinkage does not occur, and the core of the cubes is not able to densify. As a consequence, interparticle bonding is weak, thus leaving an internal cavity after removal of one of the specimens' surfaces.

This phenomenon may be the result of the combination of three mechanisms:

– differential densification rates of the outer shell and inner core due to thermal gradients in the components and volumetric expansion associated with $L1_0$ to A1 transformation
– development of gases and vapour from the debinding process
– development of by-product gases from the reduction of copper oxides/hydroxides

Dilatometric analysis (Fig. 2) detects the onset of shrinkage due to sintering already at 450–500 °C, which may not occur homogeneously in the whole component due to thermal gradients across its section. The debinding process in reducing atmosphere for the employed binder was studied in a previous work, which underlined that most of the material is removed below 450 °C, as observed in the dilatometry of the green component, and a minimal fraction cannot be burned in absence of oxygen even at higher temperatures [10]. Finally, Cu–O compounds reduction mechanisms are complex to assess, given their dependence on multiple factors, such as oxygen content in the material, hydrogen concentration, residual carbon traces, temperature and others [26].

The effect of debinding could be considered negligible since the process is almost completed below 450 °C; thus, the combination of shell sintering and gas formation from oxides reduction at high temperature should be responsible for the outcome of the process. Most likely, the sintering kinetics is fast enough to reduce the volume of open porosity in the outer region of the material whilst H_2-induced reduction is still ongoing. This may be favoured also by the volumetric increase of the particles associated to the ordered–disordered transition at about 400 °C.

Hydrogen can easily infiltrate through the porosity, but the steam generated (Eq. 7) at high temperature in the inner region remains partially trapped due to its larger specific volume, thus generating an internal pressure that prevents further shrinkage of the material, with an equivalent effect to those exploited in metal foaming processes [27–29]. Lower heating rates or intermediate steps during sintering may prove beneficial, but gas consumption would increase

significantly; thus, the study proceeded with an alternative reduction method.

$$CuO_{(s)} + H_{2(g)} \rightarrow Cu_{(s)} + H_2O_{(g)} \tag{7}$$
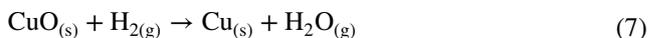
3.3 Sintering in inert atmosphere

In absence of a strong reducing agent as hydrogen, multiple mechanisms must be accounted for. First, the oxide surface layer is not stable, but undergoes a series of transformation. Whilst the core of the particles is subject to the disorder–order transformation as noted above, tenorite starts reducing forming a double layer with cuprite due to thermal decomposition. Above 600 °C, this reduction should be completed, but still stands the possibility of finding CuO at high temperature [30]. However, thermal decomposition alone is not sufficient in inert atmosphere because oxides are quite stable below 600 °C at least [23].

The possibility of sintering in inert atmosphere within a graphite crucible has been demonstrated before by Romano et al. [29] and it relies on the reduction of tenorite and cuprite by reaction with carbon at high temperature, according to the mechanisms in Eqs. 8, 9 and 10 [31, 32]:

$$2CuO + C \rightarrow Cu_2O + CO \tag{8}$$

$$CuO + CO \rightarrow Cu_2O + CO_2 \tag{9}$$

$$2Cu_2O + C \rightarrow 4Cu + CO_2 \tag{10}$$
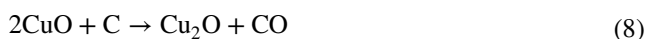
It should be noted that the components were highly densified at all temperatures, without revealing cavities such as in the cases of R800 and R830. Given the correspondence of the R800-I800 and R830-I830 cycles, it is confirmed that hydrogen plays a fundamental role in preventing full densification due to steam generation as observed above.

Optical microscopy (Fig. 5) highlights two main aspects:

• I750 presents a biphasic microstructure, whilst I800 and I830 feature a monophasic one
• Porosity is progressively reduced and density increases ($\rho_{I830} = 92.6 \pm 0.5\%$) with higher dwelling temperatures and it is mostly concentrated in the interlayer region, as described by Cabo Rios et al. [33]

Given the absence of phase transitions related to the gold alloy in the 750–800 °C range, the presence of a second phase in the I750 samples is dependent on the mechanisms of oxide reduction. EDX analysis on SEM pictures in Fig. 6 reveals that at 750 °C, the oxide coating on the particles is still present and it is responsible for the segregation of copper in this region, with a proportional enrichment in gold

Fig. 5 Optical microscopy of the polished section of the sintered **A** I750, **B** I800 and **C** I830 samples
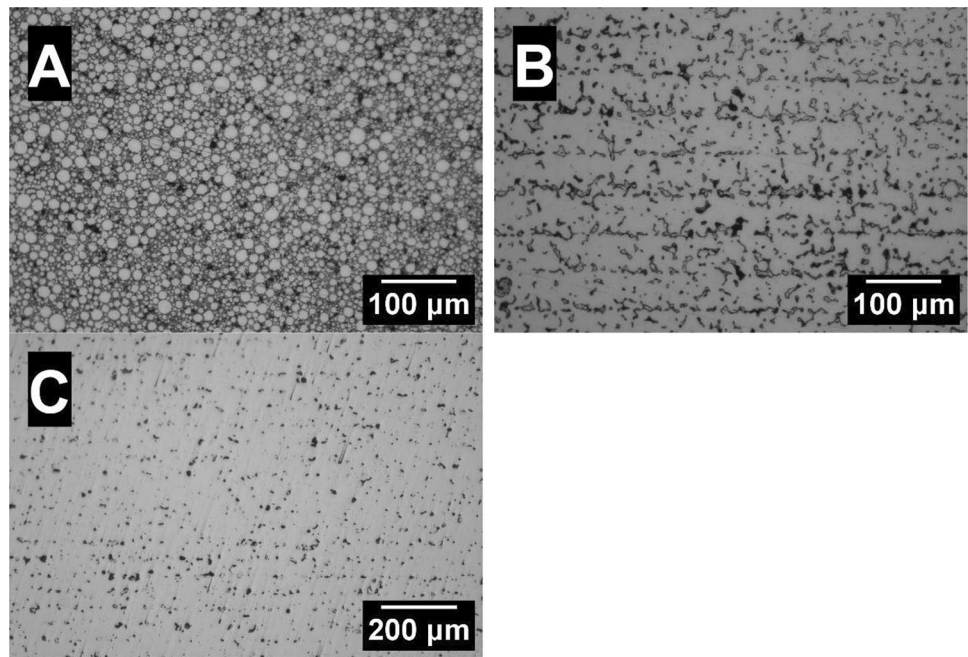
Fig. 6 Scanning electron microscopy of the section of **A** I750 and **B** I800 samples
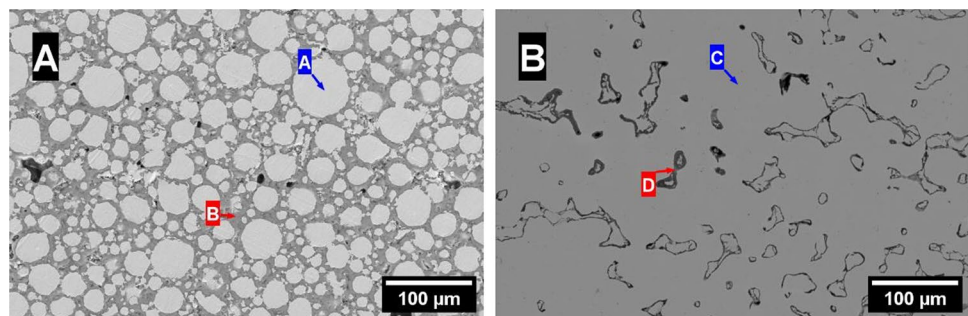
Table 3 Elemental composition from EDX analyses on gold-rich phases (A, C) and copper oxides (B, D) of I750 (A + B) and I800 (C + D) samples

Point	Au (at.%)	Cu (at.%)	Ag (at.%)	O (at.%)
A	75.2	18.1	6.7	
B		62.1		37.9
C	52.4	42.7	4.9	
D	4.2	79.1	0.6	16.0

in the core of the particles (point A), as listed in Table 3. The analysis on the oxide (point B) also reveals that it is cuprite (Cu_2O), thus it was reduced (Eqs. 8 and 9) during the treatment as expected. In I800 samples, traces of oxides can still be found in the internal surface of residual porosity (point D); however, copper oxides were mostly reduced, and the main phase (point C) featured an elemental composition closer to the nominal one.

Although the internal microstructure of I800 and I830 featured only residual traces of oxides, the presence of residual oxygen in the atmosphere induced the formation of an external oxide crust (Fig. 7) with thickness of about 1 µm (Fig. 8D) during the cooling step of the thermal cycle. A conventional treatment by immersion in pickling solution for 30 min, which is normally performed in the industry to eliminate any oxide, was sufficient to remove this layer and reveal the metallic surface beneath (Fig. 8E and F).

3.4 Case study

To demonstrate the feasibility of this technique for jewellery production, a bezel with a more complex geometry and fine details was printed and sintered with the same systems and parameters of the I830 samples. The subsequent steps of production (CAD–after curing–after sintering–after pickling) are presented in Fig. 8.

The component experienced a distortion throughout the sintering process, as can be seen from the displacement

Fig. 7 **A** Scanning electron microscopy, and **B** linear energy dispersive X-ray spectroscopy of the surface region of the I830 sample, with count per seconds graphs of **C** Au (light blue), **D** Ag (green), **E** Cu (red) and **F** O (purple)
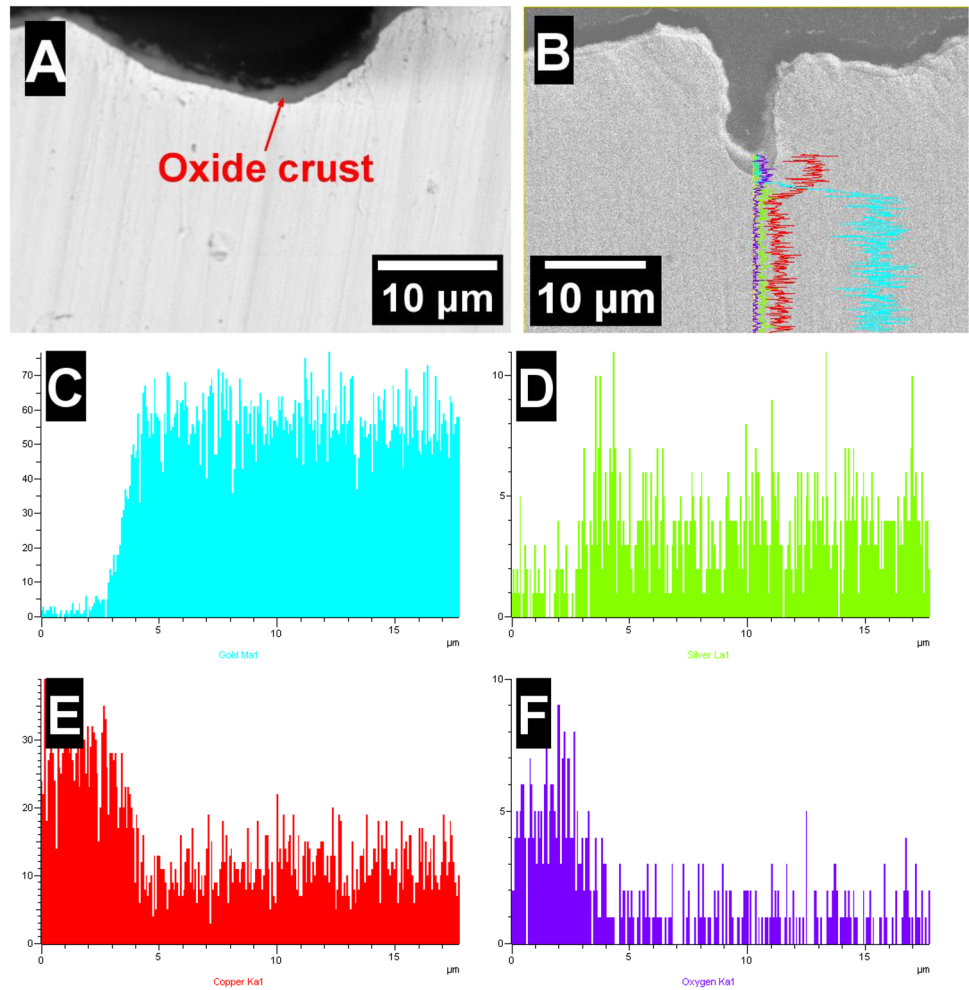
of the "8" from the central position (Fig. 8D and F). In addition, the staircase effect is evident on the side surfaces (Fig. 8E), as well as the surface roughness on the flat surfaces related to the droplet deposition direction (Fig. 8F). These kinds of defects occur frequently during densification of components by binder jetting and multiple solutions have been developed to face them, as software accounting for anisotropic shrinkage and differential volume droplets of binder at the contour of the solid to reduce the staircase effect. The surface quality can be improved as well by appropriate surface treatments as brushing, electropolishing and sandblasting [34]. In this case study, such aspect was approached by evaluating the roughness of cubic samples, and as-printed and brushed areas of the bezel surface. From Fig. 9A, it can be seen that there is a huge distinction amongst the surface quality of the areas parallel (upper) and perpendicular (side) to the powder bed plane (XY). This is due to the macroscopic porosity at the interlayer regions and it is strongly dependent on the layer thickness and the drying saturation parameters [34, 35]. The application of a post-processing treatment as polishing helps improving the quality of the surface appearance (Fig. 9B) and it could be combined with additional surface finishing operations to achieve the desired roughness [36, 37].

4 Conclusion

In this study, the feasibility of manufacturing gold alloys by binder jetting starting from a gas atomised powder was investigated and the process was applied to the production of a representative geometry for the jewellery industry.

The feedstock material proved to be suitable for the shaping phase of binder jetting, leading to the production of green bodies with a relative density close to 60%. The analysis on the curing process also revealed the presence of both ordered and disordered AuCu phases and tenorite, generated by exposure of particles to air from room temperature to 180 °C.

Fig. 8 **A**, **B** Side and top views of the bezel CAD file, **C** green sample, **D** sintered sample and **E**, **F** side and top views of the sintered samples after pickling
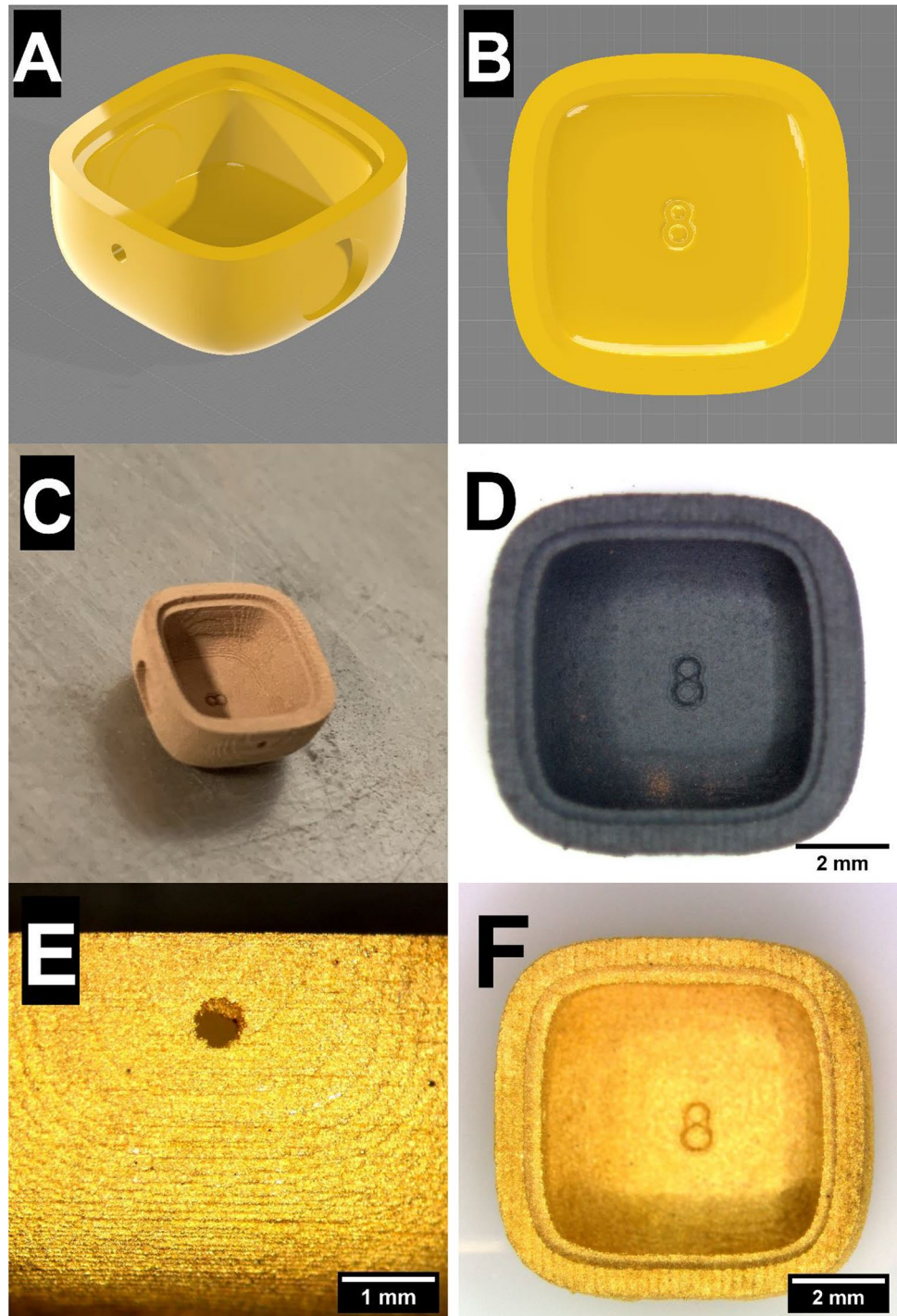
The two strategies employed to achieve densification and oxide reduction during sintering provide useful information:

1. Hydrogen containing atmospheres remove any trace of oxide from the material; however, steam by-product can build up internal pressure hindering shrinkage, thus densification.

2. Reduction of copper oxide by reaction with carbon and CO is a viable solution to remove residual oxygen from the particles, but the slower kinetics of these processes with respect to those featuring hydrogen should be considered. In our case, a dwelling temperature of 750 °C

Fig. 9 **A** R_a, R_q and R_{max} average values from measurements on the upper and side surfaces of cubic samples, **B** roughness profile curves on as-printed (straight) and brushed (dotted) surfaces of the bezel
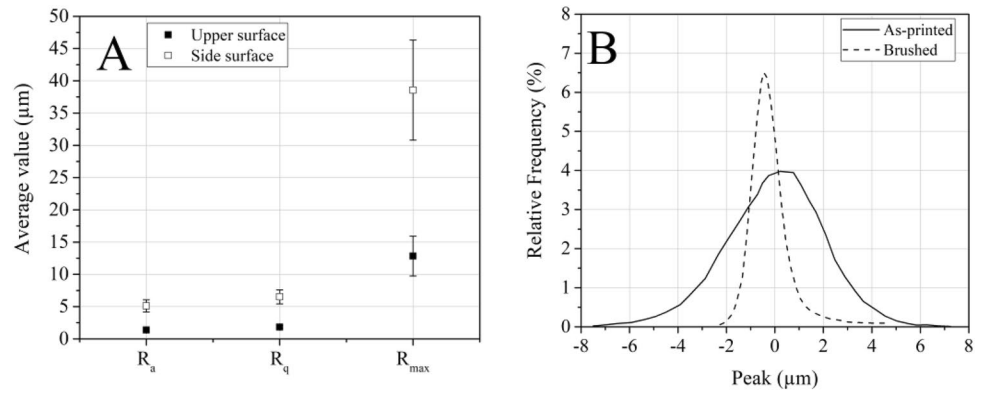
proved to be insufficient to complete reduction, whereas 800 °C led to satisfying results in samples core region with residual cuprite concentrated on the surface of the samples.

3. Higher dwelling temperature in inert atmosphere with carbon-induced oxides reduction improves densification (> 90% after sintering at 830 °C for 3 h) and residual porosity is mainly concentrated at the layers interfaces.

Further studies should focus on optimising the sintering process to avoid detrimental effects of water vapour in hydrogen-containing atmospheres, minimise oxides in case of treatment involving carbon sources and maximise density.

Data availability The project was partially supported by a commercial partner has declared in the acknowledgments and funding sections, so data cannot be made available.

References

1. Cooper F (2016) Sintering and additive manufacturing: the new paradigm for the jewellery manufacturer. Prog Addit Manuf 1:29–43. https://doi.org/10.1007/s40964-015-0003-2
2. Klotz UE, Tiberto D, Held F, Klotz UE, Tiberto D, Held F. Additive manufacturing of 18-Karat yellow-gold alloys
3. Drost E, Haußelt J (1992) Uses of gold in jewellery. Interdiscip Sci Rev 17:271–280. https://doi.org/10.1179/030801892791925448
4. Knosp H, Holliday RJ, Corti CW (2003) Gold in dentistry: alloys, uses and performance. Gold Bull 36:93–102. https://doi.org/10.1007/BF03215496
5. Khan M, Dickens P (2014) Selective laser melting (SLM) of pure gold for manufacturing dental crowns. Rapid Prototyp J 20:471–479. https://doi.org/10.1108/RPJ-03-2013-0034
6. Klotz UE, Tiberto D, Held F (2017) Optimization of 18-karat yellow gold alloys for the additive manufacturing of jewelry and watch parts. Gold Bull 50:111–121. https://doi.org/10.1007/s13404-017-0201-4
7. Ghasemi-Tabasi H, Larcher MND, Cayron C, Jhabvala J, Van Petegem S, Kalentics N et al (2022) Understanding variant selection and texture in additively manufactured red-gold alloys. Scr Mater 211:114490. https://doi.org/10.1016/j.scriptamat.2021.114490
8. Ghasemi-Tabasi H, Trtik P, Jhabvala J, Meyer M, Carminati C, Strobl M et al (2021) Mapping spatial distribution of pores in an additively manufactured gold alloy using neutron microtomography. Appl Sci 11:1–11. https://doi.org/10.3390/app11041512
9. Khan M, Dickens P (2010) Selective Laser Melting (SLM) of pure gold. Gold Bull 43:114–121. https://doi.org/10.1007/BF03214976
10. Lecis N, Mariani M, Beltrami R, Emanuelli L, Casati R, Vedani M et al (2021) Effects of process parameters, debinding and sintering on the microstructure of 316L stainless steel produced by binder jetting. Mater Sci Eng A 828:142108. https://doi.org/10.1016/j.msea.2021.142108
11. Mariani M, Goncharov I, Mariani D, De Gaudenzi GP, Popovich A, Lecis N et al (2021) Mechanical and microstructural characterization of WC-Co consolidated by binder jetting additive manufacturing. Int J Refract Met Hard Mater 100:105639. https://doi.org/10.1016/j.ijrmhm.2021.105639
12. Mariani M, Beltrami R, Brusa P, Galassi C, Ardito R, Lecis N (2021) 3D printing of fine alumina powders by binder jetting. J Eur Ceram Soc 41:5307–5315. https://doi.org/10.1016/j.jeurceramsoc.2021.04.006
13. Jiang R, Monteil L, Kimes K, Mostafaei A, Chmielus M (2021) Influence of powder type and binder saturation on

binder jet 3D-printed and sintered Inconel 625 samples. Int J Adv Manuf Technol 116:3827–3838. https://doi.org/10.1007/s00170-021-07496-3

14. Baesso I, Karl D, Spitzer A, Gurlo A, Günster J, Zocca A (2021) Characterization of powder flow behavior for additive manufacturing. Addit Manuf 47:102250. https://doi.org/10.1016/j.addma.2021.102250

15. Maximenko AL, Olumor ID, Maidaniuk AP, Olevsky EA (2021) Modeling of effect of powder spreading on green body dimensional accuracy in additive manufacturing by binder jetting. Powder Technol 385:60–68. https://doi.org/10.1016/j.powtec.2021.02.070

16. Parab ND, Barnes JE, Zhao C, Cunningham RW, Fezzaa K, Rollett AD et al (2019) Real time observation of binder jetting printing process using high-speed X-ray imaging. Sci Rep 9:2499. https://doi.org/10.1038/s41598-019-38862-7

17. Fuchs SL, Praegla PM, Cyron CJ, Wall WA, Meier C (2022) A versatile SPH modeling framework for coupled microfluid-powder dynamics in additive manufacturing: binder jetting, material jetting, directed energy deposition and powder bed fusion. https://doi.org/10.48550/arxiv.2201.01677.

18. Do T, Kwon P, Shin CS (2017) Process development toward full-density stainless steel parts with binder jetting printing. Int J Mach Tools Manuf 121:50–60. https://doi.org/10.1016/j.ijmachtools.2017.04.006

19. Grimwade M (1992) The metallurgy of gold. Interdiscip Sci Rev 17:371–381. https://doi.org/10.1179/isr.1992.17.4.371

20. Kameoka S, Tsai AP (2008) Oxidation behavior and catalytic property of intermetallic compound AuCu. Catal Today 132:88–92. https://doi.org/10.1016/j.cattod.2007.12.092

21. Garcia-Gonzalez M, Van Petegem S, Baluc N, Hocine S, Dupraz M, Lalire F et al (2019) Enhanced precipitate growth at reduced temperatures during chemical ordering in deformed red gold alloys. Scr Mater 170:129–133. https://doi.org/10.1016/j.scriptamat.2019.05.038

22. Okamoto H, Chakrabarti DJ, Laughlin DE, Massalski TB (1987) The Au-Cu (Gold-Copper) system. J Phase Equilibria 8:454–474. https://doi.org/10.1007/BF02893155

23. Goldstein EA, Mitchell RE (2011) Chemical kinetics of copper oxide reduction with carbon monoxide. Proc Combust Inst 33:2803–2810. https://doi.org/10.1016/j.proci.2010.06.080

24. Nyborg L, Cao Y (2022) Surface chemical and geometrical properties of pure copper powder intended for binder jetting and sintering. Surf Interface Anal. https://doi.org/10.1002/SIA.7107

25. Zhan W, Wang J, Wang H, Zhang J, Liu X, Zhang P et al (2017) Crystal structural effect of AuCu alloy nanoparticles on catalytic CO oxidation. J Am Chem Soc 139:8846–8854. https://doi.org/10.1021/jacs.7b01784

26. Lomello-Tafin M, Chaou AA, Morfin F, Caps V, Rousset JL (2005) Preferential oxidation of CO in H2 over highly loaded Au/ZrO2 catalysts obtained by direct oxidation of bulk alloy. Chem Commun. https://doi.org/10.1039/b413646b

27. Atwater MA, Darling KA, Tschopp MA (2016) Solid-state foaming by oxide reduction and expansion: tailoring the foamed metal microstructure in the Cu-CuO system with oxide content and annealing conditions. Adv Eng Mater 18:83–95. https://doi.org/10.1002/adem.201500063

28. Miyanaji H, Ma D, Atwater MA, Darling KA, Hammond VH, Williams CB (2020) Binder jetting additive manufacturing of copper foam structures. Addit Manuf 32:100960. https://doi.org/10.1016/j.addma.2019.100960

29. Romano T, Migliori E, Mariani M, Lecis N, Vedani M (2022) Densification behaviour of pure copper processed through cold pressing and binder jetting under different atmospheres. Rapid Prototyp J 28:1023–1039. https://doi.org/10.1108/RPJ-09-2021-0243

30. Lavrenko VA, Kuznetsova LI, Malyshevskaya AI (2005) Kinetics and mechanism of high-temperature oxidation in air of Au-Cu alloy. Powder Metall Met Ceram 44:377–381. https://doi.org/10.1007/s11106-005-0106-2

31. Liu L, Zhang TJ, Cui K, Dong YD (1999) Reduction of copper oxide with graphite by mechanical alloying. J Mater Res 14:4062–4069. https://doi.org/10.1557/JMR.1999.0548

32. Jernigan GG, Somorjai GA (1994) Carbon monoxide oxidation over three different oxidation states of copper: metallic copper, copper (I) oxide, and copper (II) oxide—a surface science and kinetic study. J Catal 147:567–577. https://doi.org/10.1006/jcat.1994.1173

33. Cabo Rios A, Hryha E, Olevsky E, Harlin P (2022) Sintering anisotropy of binder jetted 316L stainless steel: part II–microstructure evolution during sintering. Powder Metall 65:283–295. https://doi.org/10.1080/00325899.2021.2020486

34. Lores A, Azurmendi N, Agote I, Espinosa E, García-Blanco MB (2022) A study of parameter and post-processing effects on surface quality improvement of Binder Jet 3D-printed Invar36 alloy parts. Prog Addit Manuf 7:917–930. https://doi.org/10.1007/s40964-022-00267-w

35. Chen H, Zhao YF (2016) Process parameters optimization for improving surface quality and manufacturing accuracy of binder jetting additive manufacturing process. Rapid Prototyp J 22:527–538. https://doi.org/10.1108/RPJ-11-2014-0149

36. Mostafaei A, Neelapu SHVR, Kisailus C, Nath LM, Jacobs TDBB, Chmielus M (2018) Characterizing surface finish and fatigue behavior in binder-jet 3D-printed nickel-based superalloy 625. Addit Manuf 24:200–209. https://doi.org/10.1016/j.addma.2018.09.012

37. Enrique PD, Marzbanrad E, Mahmoodkhani Y, Jiao Z, Toyserkani E, Zhou NY (2019) Surface modification of binder-jet additive manufactured Inconel 625 via electrospark deposition. Surf Coatings Technol 362:141–149. https://doi.org/10.1016/j.surfcoat.2019.01.108